Tkac, O., Ma, Q., Rusher, C. A., Greaves, S. J., Orr-Ewing, A. J., & Dagdigian, P. J. (2014). Differential and integral cross sections for the rotationally inelastic scattering of methyl radicals with H-2 and D-2. The Journal of Chemical Physics, 140(20), [204318]. 10.1063/1.4879618

Link to published version (if available):
10.1063/1.4879618

Differential and integral cross sections for the rotationally inelastic scattering of methyl radicals with H_2 and D_2

Ondřej Tkáč,[1] Qianli Ma (马千里),[2] Cassandra A. Rusher,[3] Stuart J. Greaves,[3] Andrew J. Orr-Ewing,[1,a)] and Paul J. Dagdigian[2,b)]

[1] *School of Chemistry, University of Bristol, Cantock's Close, Bristol BS8 1TS, UK*

[2] *Department of Chemistry, The Johns Hopkins University, Baltimore, Maryland 21218-2685, USA*

[3] *School of Engineering and Physical Sciences, Heriot-Watt University, Edinburgh, EH14 4AS UK*

[a)] Electronic mail: a.orr-ewing@bris.ac.uk

[b)] Electronic mail: pjdagdigian@jhu.edu

Abstract

Comparisons are presented of experimental and theoretical studies of the rotationally inelastic scattering of CD_3 radicals with H_2 and D_2 collision partners at respective collision energies of 680 ± 75 and 640 ± 60 cm^{-1}. Close-coupling quantum-mechanical calculations performed using a newly constructed *ab initio* potential energy surface (PES) provide initial-to-final CD_3 rotational level ($n, k \rightarrow n', k'$) integral and differential cross sections (ICSs and DCSs). The DCSs are compared with crossed molecular beam and velocity map imaging measurements of angular scattering distributions, which serve as a critical test of the accuracy of the new PES. In general, there is very good agreement between the experimental measurements and the calculations. The DCSs for CD_3 scattering from both H_2 and D_2 peak in the forward hemisphere for $n' = 2 - 4$ and shift more to sideways and backward scattering for $n' = 5$. For $n' = 6 - 8$, the DCSs are dominated by backward scattering. DCSs for a particular CD_3 $n \rightarrow n'$ transition have a similar angular dependence with either D_2 or H_2 as collision partner. Any differences between DCSs or ICSs can be attributed to mass effects because the PES is unchanged for $CD_3 - H_2$ and $CD_3 - D_2$ collisions. Further comparisons are drawn between the $CD_3 - D_2$ scattering and results for CD_3–He presented in our recent paper [O. Tkáč, A. G. Sage , S. J. Greaves, A. J. Orr-Ewing, P. J. Dagdigian, Q. Ma, and M. H. Alexander, Chem. Sci. **4**, 4199 (2013)]. These systems have the same reduced mass, but are governed by different PESs.

I. INTRODUCTION

The potential energy surface (PES) is a key theoretical concept in the field of molecular reaction dynamics.[1] Modern quantum chemistry provides methods to compute *ab initio* PESs within the Born-Oppenheimer approximation, while measurement of state-to-state differential cross sections (DCSs) provide an excellent experimental test of the accuracy of the PES since the DCSs are sensitive to both attractive and repulsive parts of the potential.[2] The accuracy of a computed PES can hence be tested by comparing theoretical DCSs, calculated from quantum scattering theory, with experimentally measured DCSs. If theory and experiment are found to be in good agreement, robust deductions can be drawn about the collision dynamics, including the relationship between experimental measurables (*e.g.* angular distributions and state propensities) and features of the PES controlling the collision dynamics.

We focus here on DCSs involving the inelastic scattering of methyl radicals with molecular hydrogen. Studies of collisions of several important species (*e.g.* H_2O, OH, NH_3, and CH_3) with molecular hydrogen are motivated by astrophysical applications, because of the high abundance of H_2 in the universe. Collisions involving methyl radicals are of particular interest for the hydrocarbon chemistry of the atmospheres of the outer planets in the solar system,[3-5] as well as Titan.[6] Methyl radical chemistry is important in the combustion of hydrocarbons[7,8] and chemical vapour deposition of diamond films.[9,10] In addition, methyl radicals may be an integral part of a catalytic cycle for partial oxidation of methane to formaldehyde or methanol for chemical feedstocks.[11]

From a theoretical perspective, accurate close-coupling DCSs for methyl scattering are computationally tractable for collisions involving the H_2 or D_2 molecule because their large rotational constants [$B(H_2)$ = 60.853 cm^{-1} and $B(D_2)$ = 30.443 cm^{-1}][12] mean that only a few rotational levels of the collision partner need to be included in quantum scattering calculations. Although D_2 has the same mass as a He atom, collisions involving the diatomic molecule can change the internal state of both collision partners, along with the relative kinetic energy. Comparison of inelastic DCSs for collisions of methyl radicals with He, H_2, and D_2 might therefore distinguish the consequences of the additional molecular rotational degrees of freedom from purely mass related effects.

The inelastic scattering of labile free radicals was extensively reviewed in the mid 1990s,[13-15] with a focus on state-resolved integral cross sections (ICSs). Since then, experimental studies using velocity map imaging (VMI)[16,17] and laser spectroscopic detection have revolutionized measurement of state-resolved DCSs, for which the most extensively studied molecules are the NO[18-26] or OH[27-35] diatomic radicals. To date, the only reported measurement of DCSs for inelastic scattering of polyatomic free radicals is our recent study of methyl radical scattering by He.[36] We found excellent agreement between experimental measurements and DCSs calculated using the recent PES of Dagdigian and Alexander.[37] The inelastic scattering of closed-shell polyatomic molecules is more extensively illustrated by determinations of DCSs for scattering of ammonia[38-40] and deuterated ammonia[41,42] with rare gases and molecular hydrogen, and for water with helium[43] and hydrogen.[44] The rotationally inelastic scattering of deuterated methyl radicals and ammonia in collisions with helium were recently compared, using close-coupling quantum-mechanical scattering calculations performed with accurate *ab initio* PESs.[45]

Dagdigian's review of quantum scattering calculations of collisional energy transfer in small hydrocarbon intermediates provides a current perspective on polyatomic radical scattering[46] and highlights studies involving methylene (CH_2)[47,48] and methyl.[37,48,49] The energy transfer dynamics for a polyatomic species like the methyl radical are more complicated than for collisions of a diatomic molecule with an atom. In the latter case, the cylindrical symmetry limits the anisotropy to that associated with the polar angle away from the molecular axis. In contrast, for collisions of methyl radicals, anisotropies must be considered that are associated with the polar angle (away from the C_3 symmetry axis) and the azimuthal angle about this axis.

In the work reported here, DCSs for collisions of CH_3 and CD_3 with H_2 and D_2 were experimentally determined using crossed molecular beam (CMB) and VMI methods. However, we concentrate on the DCSs for collisions of CD_3 since only a few CH_3 levels can be cleanly detected because of predissociation of the excited-state used for spectroscopic detection. We compare the measured DCSs with results from quantum close-coupling scattering calculations performed using a newly computed *ab initio* PES.

II. METHOD

A. Experimental apparatus

The compact crossed molecular beam apparatus used for measurement of DCSs was described in detail previously,[36] and we present only a brief summary of the experimental method here. Schematic top and side views of the instrument were shown in Fig. 1 of Ref. 36. Molecular beams were formed by supersonic expansion through a pair of pulsed valves (General Valve Series 9) and were collimated by skimmers. The methyl radical primary molecular beam was formed by 266 nm photolysis of CH_3I or CD_3I in 3% mixtures in Ar, at a stagnation pressure of 4 bar, immediately after the orifice of the pulsed valve. The secondary molecular beam was formed by expansion of 4 bar of pure D_2 or H_2. The two skimmed beams propagated horizontally and crossed at a 90^o intersection angle in a high vacuum scattering chamber. A typical base pressure for the scattering chamber was $<10^{-8}$ Torr with the pulsed valves turned off, and this rose to $\sim10^{-7}$ Torr when the valves were operating.

The intersection region of the two molecular beams was located within a vertically mounted stack of 20 electrodes forming an ion optics assembly for dc slice-imaging.[50] A probe laser focused to the intersection of the beams ionized the scattered methyl radicals, and the electric field created by the electrode stack accelerated the ions upwards towards a position-sensitive detector. The ion detector (Photek) consisted of a pair of microchannel plates (MCPs), a phosphor screen (P46 phosphor) and a CCD camera. The voltage applied to the rear MCP was pulsed for 20 ns to time-gate the detection of ions.

UV radiation in the wavelength range 285-288 nm required for (2+1) resonance enhanced multiphoton ionization (REMPI) detection of the methyl radicals was generated by frequency doubling the output of a tuneable pulsed dye laser. The energy and linewidth of the probe laser beam were 4.5 mJ/pulse and 0.0027 nm (0.32 cm^{-1}), respectively. In our experiments, the maximum Doppler shift of inelastically scattered CD_3 radicals was 0.12 cm^{-1}, which is smaller than the laser linewidth. Methyl radicals were therefore ionized using fixed laser wavelengths chosen to probe particular rotational levels.

The electrodes forming the homogeneous acceleration field stretched the methyl ion packet along the flight axis according to the initial velocities of the neutral methyl radicals. The short voltage pulse applied to the rear MCP then allowed only a thin central slice of the ion

packet to be recorded, corresponding to methyl radicals scattered within, or close to the plane of the crossed molecular beams. Direct analysis of this slice image gave the three dimensional velocity distribution of the inelastically scattered methyl radicals without the need for image reconstruction techniques. The nozzle producing the secondary beam of pure hydrogen was operated in a repeating mode of 50 shots on and 50 shots off. The desired scattering signal was than obtained by subtraction of the background (without H_2/D_2) image from the total signal image.

Analysis of experimental images required a density-to-flux transformation because the detection efficiency of the scattered products depended on their laboratory frame velocity. To correct the images for this detection bias, we employed the method of Monte Carlo simulation of the experiment as described previously,[36] using a modification of the computer program of Eyles and Brouard.[51] Further details of the density-to-flux transformation can be found online from EPAPS.[52] Low signal levels prevented any study of laboratory-frame angular momentum polarization of the scattered methyl radicals.

B. REMPI detection and state distribution in incident beams

The methyl radical is an oblate symmetric top, with rotations described by total rotational angular momentum *n* and its body-frame projection *k*. The fine-structure and hyperfine splittings are very small[53] and are ignored in our theoretical treatment. As discussed in detail previously,[36] the CH_3 and CD_3 radicals exist in two and three nuclear spin modifications, respectively, that do not interconvert in molecular collisions. The energies of low-lying rotational levels of CH_3 and CD_3 have been plotted in Fig. 3 of Ref. 36. The normal forms (statistical mixtures of *ortho* and *para* modifications) of the H_2 and D_2 collision partners were employed in the scattering experiments.

The rotational level populations in the incident radical beam and the inelastically scattered CD_3 or CH_3 final levels were determined using (2+1) REMPI spectroscopy through the 0_0^0 band of the $4p^2A_2'' \leftarrow \widetilde{X}^2A_2''$ transition.[54,55] The level distributions in the incident radical beams were determined by comparison of experimental spectra with spectra simulated using the PGOPHER program.[56] As was shown in our recent paper,[36] the methyl radicals cooled to a

rotational temperature of ~15 K. The relative populations of the rotational levels were presented in Table 1 of Ref. 36.

The lines in the REMPI spectrum of methyl are resolved in the *n* rotational quantum number, but not in the *k* projection quantum number. Depending upon the spectroscopic branch (hence Δn of the transitions), the *k* projection levels of a given *n* contribute differently. The levels associated with the DCSs reported below are denoted by $n_{k_1 k_2 \ldots}$ to indicate that the unresolved n_{k_1}, n_{k_2}, … levels have been detected on a given transition. The relative contributions of the different *k* projection levels to the measured REMPI intensity were determined by calculating 2-photon line strength factors using the PGOPHER program.

The levels of the excited $4p^2 A_2''$ electronic state are predissociated, and the linewidths for the CH_3 isotopologue are larger than for CD_3. Hence, the efficiency of detection of CH_3 rotational levels is lower, and DCSs were determined for far fewer final levels than for CD_3. For this reason, we concentrate in this paper on the DCSs for CD_3 collisions and experimental images and DCSs for CH_3 radical can be found online from EPAPS.[52]

C. Potential energy surface

The geometry of the CH_3–H_2 rigid-rotor complex can be described by five coordinates, similar to those used in earlier work by Rist *et al*. on the NH_3–H_2 system[57] These include the intermolecular separation *R* and four angles (θ_1,ϕ_1) and (θ_2,ϕ_2) describing the orientations of the CH_3 and H_2 collision partners, respectively, relative to the Jacobian vector **R** connecting the two molecules. This body-frame coordinate system is illustrated in Fig. 1.

In order to determine the form of the angular dependence of the potential, we follow the work by Rist *et al.*[57] and consider the interaction of a symmetric top with a linear molecule as the expectation value of the sum of electrostatic interactions between the two molecules:

$$V = \langle \psi_1 \psi_2 | V | \psi_1 \psi_2 \rangle = \langle \psi_1 \psi_2 | \sum_{ij} q_i q_j r_{ij}^{-1} | \psi_1 \psi_2 \rangle \qquad (1)$$

where ψ_1 and ψ_2 are the electronic wave functions of the two molecules and q_i is the charge of particle *i*. The inverse separation between a pair *ij* of electrons can be expressed as a triple sum of modified spherical harmonics:[58]

$$r_{ij}^{-1} = \sum_{l_1 l_2 l} A_{l_1 l_2 l}(r_i, r_j, R) \sum_{m_1 m_2 m} \langle l_1 m_1 l_2 m_2 | l m \rangle C_{l_1 m_1}(\hat{r}_i) C_{l_2 m_2}(\hat{r}_j) C^*_{lm}(\Omega_{\mathrm{BS}}) \tag{2}$$

In Eq. (2), $\mathbf{r}_i$ and $\mathbf{r}_j$ are the space-fixed coordinates of the *i*th and *j*th particles of molecules 1 and 2, respectively, relative to the center of mass of each molecule. The term $\langle l_1 m_1 l_2 m_2 | l m \rangle$ is a Clebsch-Gordan coefficient, the $C_{\lambda\mu}$ are modified spherical harmonics,[59] and Ω_{BS} is the orientation of the body frame with respect to the space frame. For non-overlapping charge distributions, we must have $l = l_1+l_2$; however, l can have the full range $|l_1-l_2| \le l \le l_1+l_2$ for overlapping distributions,[60] as would be the case for an intermolecular potential.

We transform the first two spherical harmonics to the body frame[59]

$$C_{l_1 m_1}(\hat{r}_i) = \sum_{\mu_1} D^{l_1 *}_{m_1 \mu_1}(\Omega_{1\mathrm{S}}) C_{l_1 \mu_1}(\hat{\rho}_i) \tag{3}$$

and similarly for molecule 2. Substitution of Eqs. (2) and (3) into Eq. (1) and integration over the electronic coordinates yields the following formal expression for the interaction potential:

$$V(\mathbf{R}, \Omega_{1\mathrm{S}}, \Omega_{2\mathrm{S}}) = \sum_{l_1 l_2 l \mu_1 \mu_2} B_{l_1 l_2 l \mu_1 \mu_2}(R) \sum_{m_1 m_2 m} \langle l_1 m_1 l_2 m_2 | l m \rangle$$
$$\times D^{l_1 *}_{m_1 \mu_1}(\Omega_{1\mathrm{S}}) D^{l_2 *}_{m_2 \mu_2}(\Omega_{2\mathrm{S}}) C^*_{lm}(\Omega_{\mathrm{BS}}) \tag{4}$$

In Eq. (4), the B terms are radial expansion coefficients, and the $D^l_{m'm}$ are rotation matrix elements.[59] Since V is independent of the choice of the space frame, we align the space frame with the body frame (*i.e.* we align **R** along the space frame *z* axis). In this case, only $m = 0$ terms contribute to the potential. Also, only $\mu_2 = 0$ terms contribute since the electronic wave function of H_2 is cylindrically symmetric. From Fig. 1, we define the orientation between CH_3 and H_2 as follows: $\Omega_{\mathrm{B1}} \equiv (\phi_1, \theta_1, 0)$ defines the Euler angles to rotate the CH_3 molecule frame to the body frame, and $\Omega_{2\mathrm{B}} \equiv (\phi_2, \theta_2, 0)$ rotates the body frame to the H_2 molecule frame. With these considerations, we can rewrite Eq. (4) as

$$V(\mathbf{R}, \theta_1, \phi_1, \theta_2, \phi_2) = \sum_{l_1 l_2 l \mu_1} B_{l_1 l_2 l \mu_1}(R) \sum_{m_1} \langle l_1 m_1 l_2, -m_1 | l 0 \rangle$$

$$\times D^{l_1 *}_{m_1\mu_1}(0,-\theta_1,-\phi_1) D^{l_2 *}_{-m_1,0}(\phi_2,\theta_2,0) \quad (5)$$

Symmetry considerations restrict the allowed terms in Eq. (5). The three-fold symmetry of CH_3 requires that μ_1 be a multiple of 3. The potential is invariant to exchange of the hydrogen nuclei in H_2, hence l_2 must be even. Since V is real, it can be shown that

$$B_{l_1 l_2 l \mu_1}(R) = (-1)^{l_1+l_2-l+\mu_1} B^{*}_{l_1 l_2 l,-\mu_1}(R) \quad (6)$$

Since V must be invariant to reflection of H_2 through the xz plane of the CH_3 molecule frame, we have

$$B_{l_1 l_2 l,-\mu_1}(R) = (-1)^{l_1+l_2+l+\mu_1} B_{l_1 l_2 l \mu_1}(R) \quad (7)$$

Equations (6) and (7) imply that the B coefficients in Eq. (5) are real. In addition, V is invariant to reflection of H_2 through the xy plane of the CH_3 molecule frame since CH_3 is planar. It can be shown that this property restricts $l_2 + l + \mu_1$ to be even. The potential should also be invariant with respect to inversion of all coordinates; this parity invariance restricts the $l_1 + l_2 + l$ to even values.[57] However, this symmetry can be broken for the interaction of a nonlinear molecule with a diatomic.[61,62]

Substituting Eq. (7) into Eq. (5) and resolving the rotation matrix elements in Eq. (5) into products of complex exponentials and reduced rotation matrix elements, $d^{\lambda}_{\mu m}$,[59] we obtain

$$V(\mathbf{R},\theta_1,\phi_1,\theta_2,\phi_2) = \sum_{l_1 l_2 l,\mu_1 \geq 0} B_{l_1 l_2 l \mu_1}(R)(1+\delta_{\mu_1 0})^{-1} \sum_{m_1} \langle l_1 m_1 l_2,-m_1 | l 0\rangle$$
$$\times \left[e^{-i\mu_1\phi_1} d^{l_1}_{\mu_1 m_1}(\theta_1) + (-1)^{l_1+l_2+l+\mu_1} e^{i\mu_1\phi_1} d^{l_1}_{-\mu_1,m_1}(\theta_1) \right] e^{-im_1\phi_2} d^{l_2}_{-m_1,0}(\theta_2) \quad (8)$$

The PES was fitted with a modified version of Eq. (8):

$$V(\mathbf{R},\theta_1,\phi_1,\theta_2,\phi_2) = \sum_{l_1 l_2 l,\mu_1 \geq 0} C_{l_1 l_2 l \mu_1}(R) \frac{1}{2\pi} \left(\frac{[l_1][l_2]}{2} \right)^{1/2} \sum_{m \geq 0} (1+\delta_{m0})^{-1}$$
$$\times \langle l_1 m l_2,-m | l 0\rangle d^{l_2}_{-m,0}(\theta_2)$$
$$\times \left[\cos(\mu_1\phi_1 + m\phi_2) d^{l_1}_{\mu_1 m}(\theta_1) + (-1)^{l_1+l_2+l+\mu_1} \cos(\mu_1\phi_1 - m\phi_2) d^{l_1}_{-\mu_1,m}(\theta_1) \right] \quad (9)$$

where $[x] = 2x + 1$ and

$$C_{l_1 l_2 l \mu_1}(R) = \frac{4\pi}{1+\delta_{\mu_1 0}} \left(\frac{2}{[l_1][l_2]} \right)^{1/2} B_{l_1 l_2 l \mu_1}(R) \qquad (10)$$

The angular expansion in Eq. (9) is normalized so that the significance of individual terms can be evaluated directly.

We performed the explicitly correlated restricted coupled-cluster calculations with full inclusion of single and double excitations and perturbative inclusion of triple excitations [RCCSD(T)-F12a][63,64] of the CH_3–H_2 PES. We employed the aug-cc-pVTZ correlation-consistent basis sets,[65,66] with aug-cc-pVTZ/MP2FIT and cc-pVTZ/JKFIT as the density fitting basis and the resolution of identity basis, respectively.[67,68] A counterpoise correction was applied to correct for basis-set superposition error.[69] All calculations were carried out with the MOLPRO 2010.1 suite of programs.[70]

The CH_3–H_2 interaction energies were determined on a five-dimensional grid of 33 values of the intermolecular separation R [R (in bohr) = 3 – 8 in steps of 0.25; 8.5, 9, 9.5, 10, 11, 12, 13, 14, 15, 16, 18, 20]. The interaction energy was computed over a random angular grid[71] of 1,600 orientations, consisting of uniform distributions of both $\cos\theta_1$ and $\cos\theta_2$ over [–1,1] and both ϕ_1 and ϕ_2 over [0,2π]. The total number of nuclear geometries for which the interaction potential was computed was 52,800. The interaction energies for an additional 1,400 orientations at R = 5 bohr were also computed to choose statistically important terms in Eq. (9) to be used in the final fit.

These (l_1,l_2,l,μ_1) terms were chosen in the following way. We first performed a least-squares fit of the 3,000 geometries at R = 5 bohr to a large 418-term angular basis consisting of all symmetry-allowed terms with $l_1 \leq 12$ and $l_2 \leq 6$ to obtain estimated expansion coefficients for all these terms. We started from a minimal angular basis with only the isotropic term, fit the *ab initio* points, and computed the estimated fitting error e_i with a Monte Carlo error estimator.[71] We then iteratively added terms whose estimated expansion coefficients have an absolute value greater than $8e_i$, and recomputed e_i with this new angular basis until no extra terms could be included with this criterion. The total number of terms included was 55. Unlike several other PESs describing the interaction of a symmetric or an asymmetric top with a linear molecule,[62,72] all terms in our PES have even $l_1 + l_2 + l$, and none of the odd $l_1 + l_2 + l$ terms is statistically important.

The *ab initio* points were fitted using this 55-term angular basis and the least-squares method. The root mean squares (RMS) of the fit[62] increases with decreasing R but is <0.1% of the average of the absolute value $|V|$ of the potential for $R \geq 4.75$ bohr [$|V| = 2{,}500$ cm^{-1}]. Using the Monte Carlo error estimator,[71] we found the norm $\|S^{-1}\|$ for our randomly generated orientations and angular basis is 1.52. A value of $\|S^{-1}\|$ close to 1 indicates sufficient angular sampling.

Figure 2 presents a plot of the larger expansion coefficients $C_{l_1 l_2 l \mu_1}(R)$ as a function of the intermolecular separation R in the region of the van der Waals well. For the terms involving the interaction with spherically averaged H_2 (*i.e.* $l_2 = 0$), shown in the upper panel of Fig. 2, the largest coefficients are the same as for CH_3–He,[37] namely (l_1, μ_1) = (3,3) and (2,0). These reflect the leading anisotropies involving approach of the collision partner within and perpendicular to the plane of the methyl radical, as discussed previously for CH_3–He.[37] The lower panel of Fig. 2 displays the larger $C_{l_1 l_2 l \mu_1}(R)$ coefficients with $l_2 = 2$, which reflect the molecular nature of the collision partner. The plotted coefficients are direct analogs of the $l_2 = 0$ coefficients plotted in the upper panel, namely (l_1, μ_1) = (0,0), (3,3), (2,0), and (5,3), with $l = l_1 + l_2$.

The global minimum of the PES has $D_e = 99.0$ cm^{-1}, at a geometry of $R = 6.57$ bohr, $\theta_1 = 0°$, $\theta_2 = 0°$ (the ϕ angles are meaningless here). The H_2 molecule thus lies along the C_3 axis of the methyl radical above (or below, by symmetry) the molecular plane. The well depth D_e is thus significantly larger than that for CH_3–He [27.0 cm^{-1} (Ref. 37)]. The equilibrium geometry differs from that of the global minimum for CH_3–He,[37] for which the He atom lies in the molecular plane and bisects two C–H bonds.

Figure 3 presents contour plots of the dependence of the potential upon the orientation of the methyl radical for two orientations of H_2 for $R = 6.5$ bohr. For $\theta_2 = 0°$ (left-hand panel of Fig. 3) the CH_3 orientation for the most attractive interaction is the same as that of the global minimum. In this case the maximum repulsion occurs for $\theta_1 = 90°$ and $\phi_1 = 0°$, 120°, 240°; this corresponds to approach of one end of the H_2 molecule in the CH_3 plane toward one of the C–H bonds. The right-hand panel of Fig. 3 displays a contour plot of the potential for $\theta_2 = 90°$, $\phi_2 = 0°$. In this case, the most attractive CH_3 orientation ($\theta_1 = 90°$ and $\phi_1 = 60°$, 180°, 300°) corresponds to approach of the center of the H_2 molecule in the molecular plane and bisecting

two C–H bonds, with the H_2 internuclear axis lying perpendicular to the CH_3 plane. The new PES can be used without modification in scattering calculations on CD_3–H_2 and CD_3–D_2 collisions since the centers of mass are unaffected for both molecules upon isotopic substitution.

D. Quantum scattering calculations

State-to-state DCSs and ICSs for collisions of CD_3 with H_2 and D_2 were calculated using the HIBRIDON suite of programs[73] and the PES described in Sec. II.C. Rotational energies for CD_3 were computed with a rigid rotor symmetric top Hamiltonian using rotational constants from spectroscopic study by Sears *et al.*[74] Separate calculations were carried out for each nuclear spin modification of both CD_3 and H_2/D_2 since they are not interconverted in molecular collisions. The close-coupling channel basis consisted of CD_3 rotational levels whose energies were less than 960 cm^{-1} and H_2/D_2 rotational levels with $j_2 \leq 2$, and the calculations included total angular momenta $J \leq 100\ \hbar$. Convergence of the DCSs to within ~5% was checked with respect to the size of the rotational basis and the number of partial waves in the calculation. The scattering calculations used up to 5,366 channels.

Since the CD_3 incident beam contained several rotational levels, DCSs for formation of a specific final rotational level n_k were determined by weighting the computed state-to-state DCSs at the experimental collision energy by the experimentally determined incident beam rotational level populations presented in Table 1 of Ref. 36. Since the k projection number is not resolved in the REMPI spectra, computed DCSs for comparison with the experimental measurements were weighted according to the 2-photon line strengths factors for the given detection line. We assume the H_2/D_2 incident beam contains a statistical mixture of $j_2 = 0$ and 1 rotational levels and did not consider initial levels with $j_2 \geq 2$. The only j_2-changing transition included in our DCS calculations was $j_2 = 0 \rightarrow 2$. Including both the $j_2 = 0 \rightarrow 0$ and $j_2 = 0 \rightarrow 2$ transitions changes the averaged DCSs by < 10% (except for $\theta < 20^{\circ}$, an angular range obscured by the incident beam) compared to including $j_2 = 0 \rightarrow 0$ transitions alone. We expect the DCSs of other j_2-changing transitions to be even less significant due to larger energy gaps.

In previous work,[37,45,46] we examined propensities caused by the leading angular expansion coefficients of the PES in the ICSs for CH_3 and CD_3 transitions induced by collision with He. We briefly explore here these propensities for collisions of CD_3 with D_2. Figure 4

presents computed state-resolved ICSs for collision of the CD_3 1_0 level, the lowest level of A_1 nuclear spin modification, with the D_2 $j_2 = 0$ and 1 rotational levels for which j_2 is the same after the collision. These cross sections were calculated for a collision energy of 640 cm^{-1}. ICSs for transitions out of the lowest rotational levels of the A_2 and E nuclear spin modifications can be found online from EPAPS.[52]

We see in Fig. 4 that for most CD_3 transitions the ICSs for $j_2 = 1$ are only slightly larger than for $j_2 = 0$. The major exception is for the $1_0 \rightarrow 3_0$ transition, for which the cross section for $j_2 = 1$ is ~70% larger than for $j_2 = 0$, and this increase is seen in DCS for $\theta \leq 45°$. In some other molecule–H_2 systems, *e.g.* OH–H_2,[75] H_2O–H_2,[76] NH_3– H_2[77] the cross sections for the $j_2 = 1$ initial level are much larger than for $j_2 = 0$. In these systems, the collision partners of H_2 have nonzero dipole moments so that the leading electrostatic term is the dipole-quadrupole interaction. This interaction corresponds to the $l_1 = 1, l_2 = 2, l = 3$ terms and could contribute to the cross sections for the $j_2 = 1$ but not $j_2 = 0$ initial level. Since methyl has no dipole moment, this interaction is missing for CD_3–H_2/D_2. For both these systems, the transitions with the largest cross sections are to the 3_3 and 3_0 levels; the same propensities were found for collisions with He.[45] These final levels are directly coupled by the (l_1, μ_1) = (3,3) and (2,0) terms, respectively, of the PES.

III. RESULTS

Newton diagrams for inelastic scattering of CD_3 with D_2 and H_2 are shown in Fig. 5 and illustrate the laboratory frame velocities of CD_3 [$v(CD_3)$ = 550 ± 30 m s^{-1}], D_2 and H_2 [$v(D_2)$ = 2090 ± 210 m s^{-1} and $v(H_2)$ = 2950 ± 320 m s^{-1}], and the pre- and post-collision center-of-mass (CM) frame velocities of the methyl radical $u(CD_3)$ and $u'(CD_3)$, respectively. The CM-frame scattering angle θ is defined as the angle between the CM-frame velocities of CD_3 before and after a collision. The displayed Newton spheres correspond to a CD_3 transition from initial level $n_k = 0_0$ into final level $n'_{k'} = 2_0$, with an associated energy transfer of ΔE = 29 cm^{-1}, and to $\Delta j_2 = 0$ and $j_2 = 0 \rightarrow j_2' = 2$ transitions between rotational levels of D_2 and H_2.

Collision energies for inelastic scattering of CD_3 with D_2 and H_2 were 640 ± 60 and 680 ± 75 cm^{-1}, respectively. Figures 6 presents the raw images recorded for detection of CD_3 after collision with D_2. Raw images for detection of CD_3 after collision with H_2 can be found online

from EPAPS.[52] It should be noted that conservation of momentum during a collision implies that images for CD_3–H_2 scattering obtained from detection of the methyl radicals are smaller than for D_2 (and He) as a collision partner. The scattered products cannot be observed in the parts of the images closest to the forward direction because of imperfect subtraction of background signals arising from unscattered and incompletely cooled CD_3 radicals in the parent molecular beam. Asymmetry in the images about the relative velocity vector is a consequence of speed-dependent detection bias, as mentioned in Section II.A, but is corrected for by density-to-flux transformation of the data.

In most cases, more than one spectroscopic branch was probed for a given final n', giving different contributions of the unresolved k' projections with weighting according to the 2-photon line strength factors, as discussed in Sec. II.B. From examination of the images, we see that the scattering is confined relatively close to the incident beam direction for detection of low n' final levels of CD_3. This suggests that the scattering is largely in the forward direction for these levels. By contrast, the intensity shifts to larger scattering angles for high n' final levels of CD_3.

The Newton diagrams shown in Fig. 5 demonstrate that the Newton spheres for the rotational transition of D_2 from $j_2 = 0$ to $j_2' = 0$ and 2 would not be distinguishable in the measured images. Comparison of measured images for H_2 as a collision partner with the Newton diagram indicates that transitions involving rotational excitation of H_2 in a collision do not contribute significantly to the scattering, as also found in the scattering calculations (see Sec. II.D). DCSs are different for a given final level n' of CD_3 but different changes of the H_2 and D_2 rotational angular momentum; however, it is not possible to separate these types of Newton spheres from the measured images. The reason is that the experimental images result from superposition of many Newton spheres differing slightly in the magnitude and direction of the initial velocities of the collision partners and these Newton spheres are not perfectly concentric.

The recorded images were corrected with the density-to-flux transformation in order to derive the DCSs. Figure 7 displays the determined DCSs for CD_3–D_2 for final levels $n' = 2 – 4$, while Fig. 8 presents the DCSs for $n' = 5 – 7$. Also plotted in Figs. 7 and 8 are the theoretical DCSs. The experimental and calculated DCSs for the CD_3–H_2 system are shown in Fig. 9 for final levels $n' = 2 – 4$ and in Fig. 10 for $n' = 5 – 8$. For quantitative comparison with the theoretical calculations, the experimental DCSs were normalized by scaling the experimental

value at 60° scattering angle to match the theoretical value at that angle. Since the scattering is mainly into the backward hemisphere for large Δn transitions, the DCSs for the $R(7)$ and $P(8)$ lines for collision with H_2 were normalized at 90°.

The experimental DCSs are not shown for $\theta < 30°$ for final levels with $n' = 2$ and 3 and for $\theta < 20°$ for final levels with higher n' because of contributions to these angles from unscattered radicals in the parent beam. The calculated DCSs show pronounced diffraction oscillations in this strongly forward scattered region, but the angular resolution of the experiments would be insufficient to resolve these structures clearly, even with greater initial state purity. The angular resolution is limited by the velocity and angular spreads of the two molecular beams, and for the current experiments on the $CD_3 + D_2/H_2$ systems, varies from 3 to 18° depending on the scattering angle.[36]

The error bars associated with the experimental DCSs were determined by combining the standard deviation determined from comparison of several measured images for a single final state with the uncertainty introduced by application of the density-to-flux transformation. The latter factor was quantified by comparing DCSs extracted from the two halves of the image separated by the relative velocity vector (which should be symmetric after perfect transformation).

There is generally quantitative agreement between the (normalized) experimental and computed DCSs, although some small discrepancies are evident for scattering angles < 45° for some probe transitions with $n' \leq 4$. Here, the experimental DCSs are slightly larger than the computed DCSs, which could be a consequence of our limited experimental angular resolution or imperfect background subtraction. There may also be contributions to the scattering signals from initial levels with higher initial n present at low density in our ~15 K beam, because elastic scattering events will give strong forward scattering with high integral cross sections. The only significant differences between the experimental and computed DCSs are for detection of some high-n' final rotational levels, in particular via the $S(5)$ and $S(6)$ lines in collisions with D_2 and the $R(5)$ and $S(5)$ lines in collisions with H_2. Even for these cases, there is satisfactory qualitative agreement between the shapes of the experimental and computed DCSs.

IV. DISCUSSION

Although the focus of our study is on inelastic scattering, the collision of a methyl radical with molecular hydrogen can also follow a reactive pathway. However, the vibrationally adiabatic barrier height on the potential energy surface for reactive formation of methane and atomic hydrogen has been computed to be 3847 cm^{-1}.[78] This energy barrier is much higher than the collision energy in our experiments and calculations so the reactive path is closed. Moreover, the PES was computed with the assumption of rigid molecular geometries. Our comparisons of experimental and computed DCSs therefore test the quality of the *ab initio* PES and the accuracy of the scattering calculation methods in regions of the global PES below the transition state for reaction.

For both D_2 and H_2 as collision partners, the measured images and the corresponding DCSs directly reveal the dependence of the scattering upon CD_3 final rotational angular momentum n'. The DCSs peak in the forward hemisphere for $n' = 2 - 4$ and shift more to sideways and backward scattering for $n' = 5$. For $n' = 6 - 8$, the DCSs are dominated by backward scattering. A similar trend was observed for scattering of methyl radicals with He, and we discussed the origins of this behavior in terms of partial cross sections (or impact-parameter dependence of the scattering) in a recent paper.[36] DCSs were measured for different spectroscopic branches to probe a given methyl rotational level n', but a different subset of the k'-projection quantum numbers. These DCSs differ, especially for $n' = 5$, demonstrating the sensitivity of scattering to the k' value, even if it is not fully resolved in the current experiments.

With inspection of Figs. 7 – 10, we see that there are a few clear differences between DCSs measured for H_2 and D_2 as collision partners with CD_3, the most apparent being that the DCSs for the CD_3–D_2 system decrease more sharply from a maximum at small scattering angles towards larger angles. In view of the good agreement between the experimental and computed DCSs, we can compare in detail computed state-resolved DCSs for the two systems. It should be noted that we have no clear experimental information on the rotational inelasticity of the D_2/H_2 collision partner.

Figure 11 compares the DCSs for transitions from the CD_3 1_0 rotational level, the lowest level of A_1 nuclear spin modification, into selected final levels in collisions with D_2 and H_2 at relative translational energies of 640 and 680 cm^{-1}, respectively. State-to-state ICSs

corresponding to the DCSs plotted in Fig. 11 are displayed in Fig. 4 for D_2 as a collision partner. DCSs for transitions involving other final levels and for collisions out of the 0_0 and 1_1 rotational levels, the lowest levels of the A_2 and E nuclear spin modifications, respectively, can be found online from EPAPS.[52] We see in Fig. 11 that DCSs for the same transitions have a similar angular dependence for the D_2 and H_2 collision partners. For final levels $n' \leq 4$, the DCSs for the D_2 collision partner are larger for small angles, while the DCSs for H_2 extend to larger scattering angles than do the DCSs for D_2. For intermediate states ($n' = 5$ and 6), the DCSs for D_2 are dominated by sideways scattering with peaks around $\theta \sim 90°$, whereas the DCSs for H_2 are shifted more to backward hemisphere. The DCSs for higher final levels are dominated by backward scattering for both collision partners as demonstrated in Fig. 11 by DCSs for the 7_0 final level. We notice that the CD_3–D_2 DCSs are very similar for the D_2 $j_2 = 0$ and 1 initial rotational levels. The DCSs for the $j_2 = 0 \rightarrow 2$ transition (not plotted) are in general more backward scattered for H_2 than for D_2 for small Δn changes ($n' \leq 5$) and have the same angular dependence for larger Δn changes. In addition, for a given CD_3 transition, the ratio of the ICSs for the $j_2 = 0 \rightarrow 2$ to the $j_2 = 0 \rightarrow 0$ transition is much smaller for the H_2 collision partner than for D_2; this is presumably due to the larger energy gap for $\Delta j_2 = 2$ transition in H_2. The PESs for CD_3–D_2 and CD_3–H_2 scattering are identical, so observed differences in DCSs must be attributed to the effects of different masses of the collider, and any associated changes to the quantized rotational energy levels of H_2 and D_2.

Conversely, collisions of CD_3 with D_2 and He have the same reduced mass, but are governed by different PESs. A further difference between He and D_2 collision partners is that D_2 has a rotational degree of freedom, so can be rotationally excited or de-excited in a collision, and collisions can also occur with an initially rotationally excited molecule. In our experiments (present work and Ref. 36), the D_2 molecular beam has a larger mean speed than does the He beam (because of the larger heat capacity ratio for a monatomic gas ($\gamma = 5/3$) than for a diatomic gas ($\gamma = 7/5$)). To make a clear comparison of these two systems, we have calculated CD_3–He DCSs at the same collision energy (and hence relative velocity) as the present experiments on CD_3–D_2. Figure 12 presents computed DCSs for selected transitions from the 1_1 rotational level, the lowest level of the E nuclear spin modification, for CD_3 in collisions with D_2 and He at a collision energy of 640 cm^{-1}. Each DCS depicted represents an example of a transition

directly coupled by one of the largest expansion coefficients of the PES for the CD_3–He system (see Fig. 3 in Ref. 45). For the D_2 collision partner, DCSs are presented for initial rotational levels $j_2 = 0$ and 1, with no collision-induced change in j_2. DCSs for a wider range of CD_3 initial and final rotational levels can be found online from EPAPS.[52] The DCSs for initial $j_2 = 1$ of D_2 are often larger, in particular in the forward direction (note the scaling of the $j_2 = 1 \rightarrow 1$ DCS in Fig. 12(a)).

The CD_3–D_2 DCSs show similar propensities for changes in the CD_3 rotational quantum numbers n and k as for CD_3–He collisions.[36] For small changes Δn in the rotational angular momentum, the DCSs for $\Delta k = 0$ transitions have fairly sharp forward peaks and broad, lower intensity peaks in the backward hemisphere (Fig. 12(a)). These transitions are enabled mainly by the $(l_1, \mu_1) = (2,0)$ terms, in a similar fashion to the role of the v_{20} term for CD_3–He.[37] The $\Delta k \neq 0$ transitions for small Δn changes display broad DCSs extending over the entire angular range, with oscillations for angles $\theta \leq 45°$ (Fig. 12(b)). Such transitions involve direct coupling through the $(l_1, \mu_1) = (3,3)$ terms, in analogy to the role of the v_{33} term for CD_3–He.[37] The $\Delta k = 1$ transitions for the E nuclear spin modification, *e.g.* the $1_1 \rightarrow 3_2$ transition in panels (b), have DCSs very similar in shape to those for $\Delta k = 3$ transitions for A_1 and A_2 levels *e.g.* the $0_0 \rightarrow 3_3$ transition. As discussed in detail previously for CD_3–He,[36,37,45] these $\Delta k \neq 0$ transitions for E levels are also enabled by the $(l_1, \mu_1) = (3,3)$ terms. For transitions with larger changes in the rotational quantum number n, the DCSs shift toward the backward hemisphere, as can be seen in the comparison of experimental and computed DCSs displayed in Figs. 8 and 10 for D_2 and H_2 collision partners, respectively.

V. CONCLUSIONS

The experimental measurements reported here of inelastic scattering of CD_3 radicals with H_2 and D_2 molecules represent the first DCSs obtained for collisions of a polyatomic radical with a diatomic molecule. We have compared these experimental DCSs with the outcomes of close coupling quantum-mechanical calculations performed using a newly determined *ab initio* PES computed at the RCCSD(T)-F12a level of theory. We find good agreement between the experimental and calculated DCSs, with the exception of scattering into the $n' = 5$ and 6 levels of CD_3, as probed by the $S(5)$ and $S(6)$ REMPI lines in collisions with D_2 and the $R(5)$ and $S(5)$

lines in collisions with H_2. This agreement suggests that the PES and the scattering calculations provide an accurate description of the interaction of CD_3 with these diatomic molecules, at least at energies around 600–700 cm^{-1} corresponding to our experimental conditions.

The DCSs for inelastic scattering of CD_3 with H_2 and D_2 peak in the forward hemisphere for $n' = 2 - 4$ and shift more to sideways and backward scattering for $n' = 5$. As the energy transfer in a collision increases, the DCSs are increasingly dominated by backward scattering ($n' = 6 - 8$). This same behavior is recognized for inelastic scattering of diatomic and polyatomic molecules and it is also consistent with our prior report[36] of inelastic scattering of CD_3 with He. DCSs for a given n, $k \rightarrow n'$, k' transition show similar angular dependences for D_2 and H_2 as collision partners. Since CD_3–D_2 and CD_3–H_2 interactions are described by the same PES, small differences between DCSs or ICSs for D_2 and H_2 collision partners can be attributed to mass effects, or, in the case of transitions involving a change in the rotational angular momentum of the diatomic collider, to mass-related changes in the quantized energy level structure.

We also computed rotational-level resolved integral cross sections for collision of CD_3 with D_2 and H_2. The ICSs for inelastic scattering of CD_3 with D_2 and H_2 $j_2 = 1$ are larger than for $j_2 = 0$, indicating that an initially rotating D_2 or H_2 molecule increases the probability of a given CD_3 transition. The ratio of ICSs for $j_2 = 0 \rightarrow 2$ to $j_2 = 0 \rightarrow 0$ transitions in the diatomic, for a particular change in the CD_3 angular momentum, is much smaller for H_2 than for D_2 because of the larger energy gap between rotational levels of the lighter isotopologue. CD_3–D_2 DCSs are very similar for collisions with D_2 initially in $j_2 = 0$ and 1 rotational levels.

We also compare the DCSs for CD_3–D_2 with CD_3–He measured previously.[36] Comparison of these systems is interesting because they have the same reduced mass, but the scattering dynamics of CD_3 with D_2 and He is governed by different PESs, and thus the forces acting between the collision partners. For example, the global minimum of the CD_3–D_2 PES has D_e = 99.0 cm^{-1}, which is significantly larger than for CD_3–He [27.0 cm^{-1} (Ref. 37)]. The equilibrium geometry for CD_3–D_2 is R = 6.57 bohr, $\theta_1 = 0°$, $\theta_2 = 0°$. The D_2 molecule thus lies along the C_3 axis of the methyl radical as opposed to the equilibrium geometry of the global minimum for CD_3–He, for which the He atom lies in the molecular plane and bisects two C–H bonds at R = 6.52 bohr.

When comparisons are made between computed DCSs for CD_3–D_2 and CD_3–He scattering at the same collision energy, we find a similar dependence on scattering angle. This observation is particularly the case for transitions directly coupled by terms representing the three-fold anisotropy associated with the azimuthal angle about the C_3 symmetry axis of the radical. ICS for CD_3-He and CD_3–D_2, in which the D_2 is in an initial level with $j_2 = 0$, are of comparable magnitudes.

Acknowledgements

The Bristol group acknowledges financial support from the EPSRC Programme Grant EP/G00224X and from the EU Marie Curie Initial Training Network *ICONIC* (for an Early Career Researcher position for OT). The Heriot-Watt group thanks EPSRC for support via grant EP/J002534/2. The theoretical portion of this work was supported by the Chemical, Geosciences and Biosciences Division, Office of Basic Energy Sciences, Office of Science, U.S. Department of Energy, under Grant No. DESC0002323. The authors gratefully acknowledge the encouragement and advice of Millard Alexander.

References

1. *Tutorials in Molecular Reaction Dynamics*, edited by M. Brouard and C. Valance (Royal Society of Chemistry, Cambridge, UK, 2010).
2. M. S. Child, *Molecular Collision Theory* (Academic Press INC. LTD., London and New York, 1974).
3. B. Bezard, H. Feuchtgruber, J. Moses, and T. Encrenaz, Astron. Astrophys. **334**, L41 (1998).
4. B. Bezard, P. N. Romani, H. Feuchtgruber, and T. Encrenaz, Astrophys. J. **515**, 868 (1999).
5. J. I. Moses, B. Bezard, E. Lellouch, G. R. Gladstone, H. Feuchtgruber, and M. Allen, Icarus **143**, 244 (2000).
6. Y. L. Yung and W. B. DeMore, *Photochemistry of Planetary Atmospheres* (Oxford University Press, New York, Oxford, 1997).
7. J. A. Miller, R. J. Kee, and C. K. Westbrook, Annu. Rev. Phys. Chem. **41**, 345 (1990).
8. *Gas-Phase Combustion Chemistry*, edited by W. C. Gardiner Jr. (Springer, New York, 2000).
9. P. W. May, N. L. Allan, M. N. R. Ashfold, J. C. Richley, and Y. A. Mankelevich, J. Phys.: Condensed Matter **21**, 364203 (2009).
10. S. J. Harris, Appl. Phys. Letters **56**, 2298 (1990).
11. H. F. Liu, R. S. Liu, K. Y. Liew, R. E. Johnson, and J. H. Lunsford, J. Am. Chem. Soc. **106**, 4117 (1984).
12. K. P. Huber and G. Herzberg, *Molecular Spectra and Molecular Structure IV. Constants of Diatomic Molecules* (Van Nostrand Reinhold, Princeton, 1979).
13. P. J. Dagdigian, in *The Chemical Dynamics and Kinetics of Small Radicals, Part I*, edited by K. Liu and A. F. Wagner (World Scientific, Singapore, 1995), p. 315.
14. J. C. Whitehead, Rept. Prog. Phys. **59**, 993 (1996).
15. A. Schiffman and D. W. Chandler, Int. Rev. Phys. Chem. **14**, 371 (1995).
16. D. W. Chandler and P. L. Houston, J. Chem. Phys. **87**, 1445 (1987).
17. A. Eppink and D. H. Parker, Rev. Sci. Instrum. **68**, 3477 (1997).
18. F. J. Aoiz, J. E. Verdasco, M. Brouard, J. Kłos, S. Marinakis, and S. Stolte, J. Phys. Chem. A **113**, 14636 (2009).

19. M. Brouard, H. Chadwick, C. J. Eyles, B. Hornung, B. Nichols, F. J. Aoiz, P. G. Jambrina, S. Stolte, and M. P. de Miranda, J. Chem. Phys. **138**, 104309 (2013).
20. M. Brouard, H. Chadwick, C. J. Eyles, B. Hornung, B. Nichols, F. J. Aoiz, P. G. Jambrina, and S. Stolte, J. Chem. Phys. **138**, 104310 (2013).
21. C. J. Eyles, M. Brouard, H. Chadwick, F. J. Aoiz, J. Kłos, A. Gijsbertsen, X. Zhang, and S. Stolte, Phys. Chem. Chem. Phys. **14**, 5420 (2012).
22. C. J. Eyles, M. Brouard, H. Chadwick, B. Hornung, B. Nichols, C. H. Yang, J. Kłos, F. J. Aoiz, A. Gijsbertsen, A. E. Wiskerke, and S. Stolte, Phys. Chem. Chem. Phys. **14**, 5403 (2012).
23. C. J. Eyles, M. Brouard, C. H. Yang, J. Kłos, F. J. Aoiz, A. Gijsbertsen, A. E. Wiskerke, and S. Stolte, Nature Chem. **3**, 597 (2011).
24. J. J. Kay, J. D. Steill, J. Kłos, G. Paterson, M. L. Costen, K. E. Strecker, K. G. McKendrick, M. H. Alexander, and D. W. Chandler, Mol. Phys. **110**, 1693 (2012).
25. J. Kłos, F. J. Aoiz, J. E. Verdasco, M. Brouard, S. Marinakis, and S. Stolte, J. Chem. Phys. **127**, 031102 (2007).
26. H. Kohguchi, T. Suzuki, and M. H. Alexander, Science **294**, 832 (2001).
27. M. Kirste, L. Scharfenberg, J. Kłos, F. Lique, M. H. Alexander, G. Meijer, and S. Y. T. van de Meerakker, Phys. Rev. A **82**, 042717 (2010).
28. S. Marinakis, G. Paterson, J. Kłos, M. L. Costen, and K. G. McKendrick, Phys. Chem. Chem. Phys. **9**, 4414 (2007).
29. G. Paterson, S. Marinakis, M. L. Costen, K. G. McKendrick, J. Kłos, and R. Tobola, J. Chem. Phys. **129**, 074304 (2008).
30. Z. Pavlovic, T. V. Tscherbul, H. R. Sadeghpour, G. C. Groenenboom, and A. Dalgarno, J. Phys. Chem. A **113**, 14670 (2009).
31. K. Schreel, J. Schleipen, A. Eppink, and J. J. ter Meulen, J. Chem. Phys. **99**, 8713 (1993).
32. M. Brouard, A. Bryant, Y. P. Chang, R. Cireasa, C. J. Eyles, A. M. Green, S. Marinakis, F. J. Aoiz, and J. Klos, J. Chem. Phys. **130**, 044306 (2009).
33. M. Brouard, H. Chadwick, Y. P. Chang, C. J. Eyles, F. J. Aoiz, and J. Kłos, J. Chem. Phys. **135**, (2011).
34. L. Scharfenberg, K. B. Gubbels, M. Kirste, G. C. Groenenboom, A. van der Avoird, G. Meijer, and S. Y. T. van de Meerakker, Eur. Phys. J. D **65**, 189 (2011).
35. M. C. van Beek, J. J. ter Meulen, and M. H. Alexander, J. Chem. Phys. **113**, 628 (2000).
36. O. Tkáč, A. K. Sage , S. J. Greaves, A. J. Orr-Ewing, P. J. Dagdigian, Q. Ma, and M. H. Alexander, Chem. Sci. **4**, 4199 (2013).

37. P. J. Dagdigian and M. H. Alexander, J. Chem. Phys. **135**, 064306 (2011).
38. G. Ebel, R. Krohne, H. Meyer, U. Buck, R. Schinke, T. Seelemann, P. Andresen, J. Schleipen, J. J. ter Meulen, and G. H. F. Diercksen, J. Chem. Phys. **93**, 6419 (1990).
39. H. Meyer, J. Chem. Phys. **101**, 6686 (1994).
40. H. Meyer, J. Phys. Chem. A **99**, 1101 (1995).
41. J. J. Kay, S. Y. T. van de Meerakker, E. A. Wade, K. E. Strecker, and D. W. Chandler, J. Phys. Chem. A **113**, 14800 (2009).
42. O. Tkáč, A. K. Saha, J. Onvlee, C.-H. Yang, G. Sarma, C. K. Bishwakarma, S. Y. T. van de Meerakker, A. van der Avoird, D. H. Parker, and A. J. Orr-Ewing, Phys. Chem.Chem. Phys. **16**, 477 (2014).
43. C. H. Yang, G. Sarma, J. J. ter Meulen, D. H. Parker, U. Buck, and L. Wiesenfeld, J. Phys. Chem. A **114**, 9886 (2010).
44. C. H. Yang, G. Sarma, D. H. Parker, J. J. ter Meulen, and L. Wiesenfeld, J. Chem. Phys. **134**, 204308 (2011).
45. O. Tkáč, A. J. Orr-Ewing, P. J. Dagdigian, M. H. Alexander, J. Onvlee, and A. van der Avoird, J. Chem. Phys. (submitted) (2014).
46. P. J. Dagdigian, Int. Rev. Phys. Chem. **32**, 229 (2013).
47. L. Ma, M. H. Alexander, and P. J. Dagdigian, J. Chem. Phys. **134**, 154307 (2011).
48. L. Ma, P. J. Dagdigian, and M. H. Alexander, J. Chem. Phys. **136**, 224306 (2012).
49. Q. Ma, P. J. Dagdigian, and M. H. Alexander, J. Chem. Phys. **138**, 104317 (2013).
50. D. Townsend, M. P. Minitti, and A. G. Suits, Rev. Sci. Instrum. **74**, 2530 (2003).
51. C. J. Eyles, Ph. D. thesis, University of Oxford (2010).
52. See Supplementary Material Document No._____ for details on the density-to-flux transformation, raw images for the CD_3-H_2 and CH_3-H_2/D_2 systems, derived DCSs for CH_3 scattering, and more plots of state-resolved integral and differential cross sections. For information on Supplementary Material, see http://www.aip.org/pubservs/epaps.html.
53. S. Davis, D. T. Anderson, G. Duxbury, and D. J. Nesbitt, J. Chem. Phys. **107**, 5661 (1997).
54. I. Powis and J. F. Black, J. Phys. Chem. A **93**, 2461 (1989).
55. J. F. Black and I. Powis, J. Chem. Phys. **89**, 3986 (1988).
56. PGOPHER, a Program for Simulating Rotational Structure, C. M. Western, University of Bristol, http://pgopher.chm.bris.ac.uk.
57. C. Rist, M. H. Alexander, and P. Valiron, J. Chem. Phys. **98**, 4662 (1993).
58. C. G. Gray, Can. J. Phys. **54**, 505 (1976).

59. D. M. Brink and G. R. Satchler, *Angular Momentum,* 2nd ed. (Clarendon Press, Cambridge, UK, 1968).
60. H. J. Silverstone, Adv. Quantum Chem. **86**, 3 (2014).
61. S. Green, J. Chem. Phys. **103**, 1035 (1995).
62. P. Valiron, M. Wernli, A. Faure, L. Wiesenfeld, C. Rist, S. Kedžuch, and J. Noga, J. Chem. Phys. **129**, 134306 (2008).
63. T. B. Adler, G. Knizia, and H.-J. Werner, J. Chem. Phys. **127**, 221106 (2007).
64. G. Knizia, T. B. Adler, and H.-J. Werner, J. Chem. Phys. **130**, 054104 (2009).
65. T. H. Dunning, Jr., J. Chem. Phys. **90**, 1007 (1989).
66. R. A. Kendall, T. H. Dunning, Jr., and R. J. Harrison, J. Chem. Phys. **96**, 6796 (1992).
67. F. Weigend, A. Köhn, and C. Hättig, J. Chem. Phys. **116**, 3175 (2002).
68. F. Weigend, Phys. Chem. Chem. Phys. **4**, 4285 (2002).
69. F. B. van Duijneveldt, J. G. C. M. van Duijneveldt-van de Rijdt, and J. H. van Lenthe, Chem. Rev. **94**, 1873 (1994).
70. MOLPRO, version 2010.1, a package of ab initio programs, H.-J. Werner, P. J. Knowles, R. Lindh, F. R. Manby, M. Schütz, and others, see http://www.molpro.net.
71. C. Rist and A. Faure, J. Math. Chem. **50**, 588 (2012).
72. A. Spielfiedel, M.-L. Senent, F. Dayou, C. Balança, L. Cressiot-Vincent, A. Faure, L. Wiesenfeld, and N. Feautrier, J. Chem. Phys. **131**, 014305 (2009).
73. HIBRIDON is a package of programs for the time-independent quantum treatment of inelastic collisions and photodissociation written by M. H. Alexander, D. E. Manolopoulos, H.-J. Werner, B. Follmeg, P. J. Dagdigian, Q. Ma, and others. More information and/or a copy of the code can be obtained from the website http://www2.chem.umd.edu/groups/physical/hibridon/.
74. T. J. Sears, J. M. Frye, V. Spirko, and W. P. Kraemer, J. Chem. Phys. **90**, 2125 (1989).
75. K. Schreel and J. J. t. Meulen, J. Chem. Phys. **105**, 4522 (1996).
76. A. Faure, N. Crimier, C. Ceccarelli, P. Valiron, L. Wiesenfeld, and M. L. Dubernet, Astron. Atrophys. **472**, 1029 (2007).
77. S. Maret, A. Faure, E. Scifoni, and L. Wiesenfeld, Mon. Not. R. Astron. Soc. **399**, 425 (2009).
78. D. Y. Wang, J. Chem. Phys. **117**, 9806 (2002).

Figures

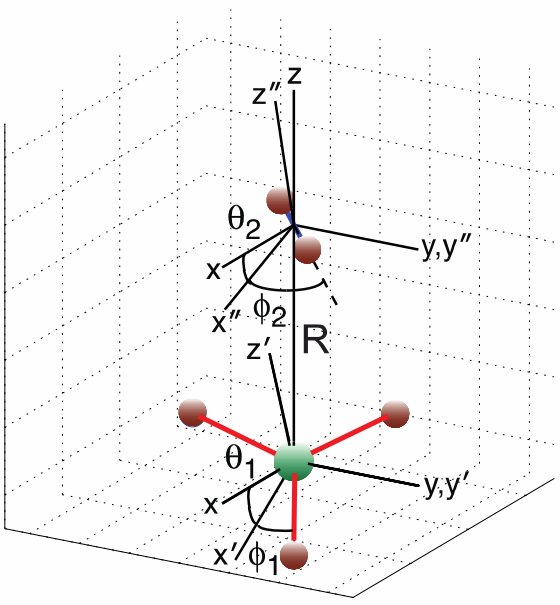

FIG. 1. Body-frame coordinate system to specify the geometry of the CH_3–H_2 complex. The Jacobian **R** vector lies along the z axis. The CH_3 and H_2 molecule-frame axes are denoted by (x', y', z') and (x'', y'', z''), respectively.

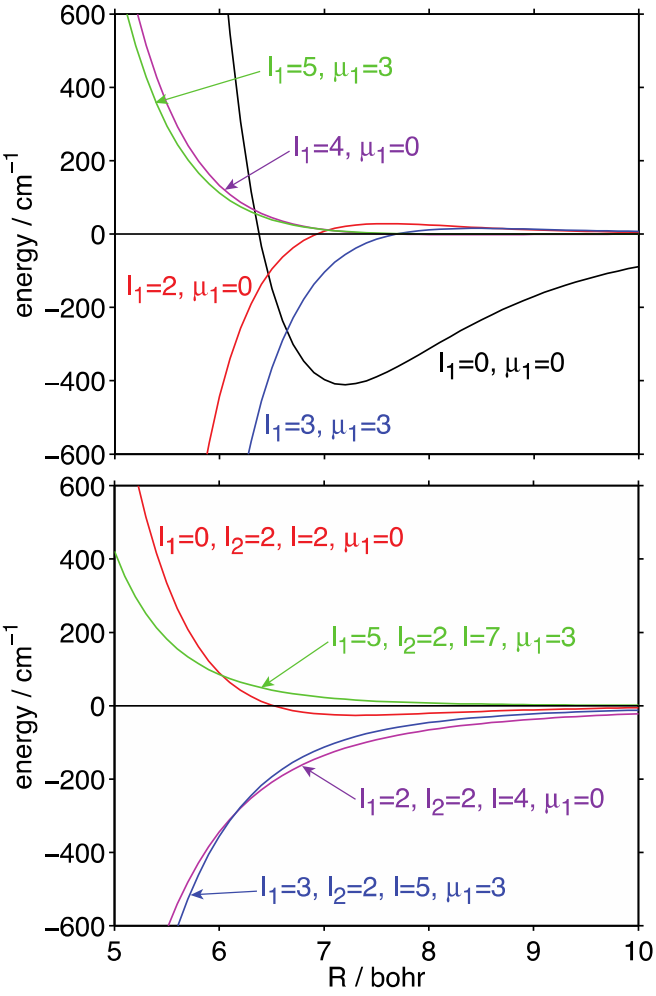

FIG. 2. Dependence of the larger expansion coefficients $C_{l_1 l_2 l \mu_1}(R)$ [defined in Eq. (9)] upon the CH_3–H_2 separation R. Upper panel: coefficients with $l_2 = 0$ (and hence $l = l_1$); lower panel: coefficients with $l_2 = 2$. The expansion coefficients are the same for the interaction of CH_3 or CD_3 with D_2 since the centers of mass of the hydrogen molecule and methyl radical do not change under isotopic substitution.

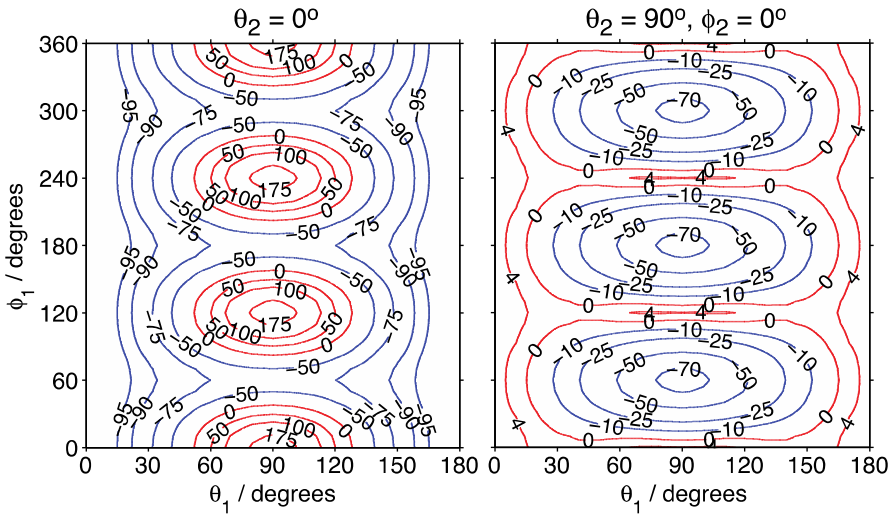

FIG. 3. Dependence of the potential energy (in cm^{-1}) on the orientation (θ_1, ϕ_1) of the methyl radical for two orientations (θ_2, ϕ_2) of the H_2 collision partner for an intermolecular separation R = 6.5 bohr. The ϕ_2 angle is meaningless in the left-hand panel, with $\theta_2 = 0°$.

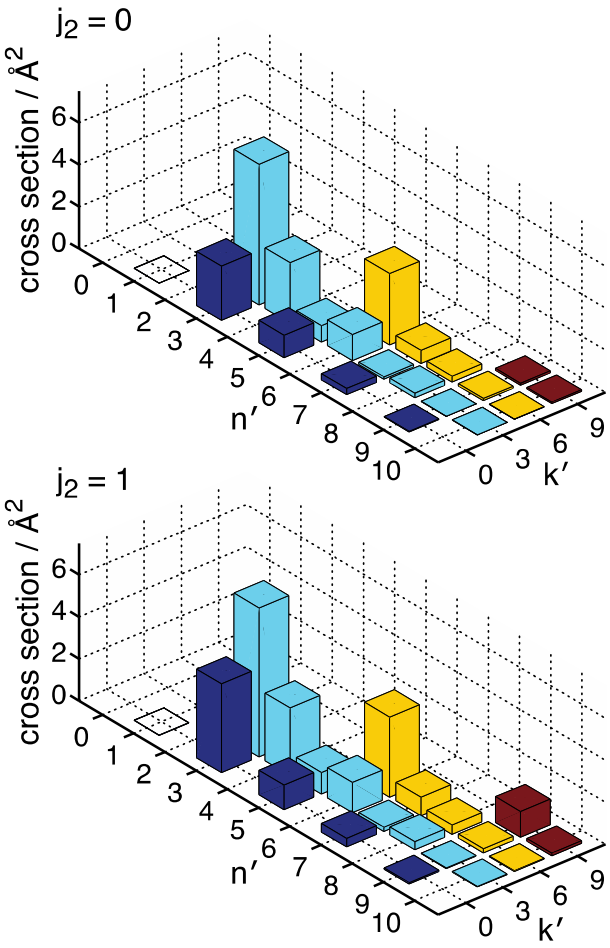

FIG. 4. ICSs for transitions out of the CD_3 1_0 level (the lowest level of the A_1 nuclear spin modification) in collisions with D_2 at a relative translational energy of 640 cm^{-1}. The rotational level of the collision partner is $j_2 = 0$ (upper panel) and $j_2 = 1$ (lower panel). The initial level is indicated with an open square. Since the cross sections for transitions to CD_3 high n levels are small, the plots show cross sections for final levels with $n' \leq 10$.

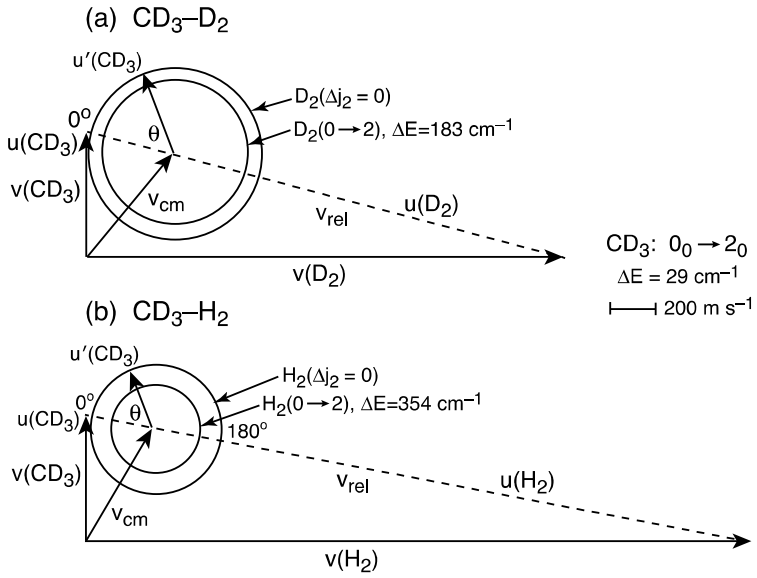

FIG. 5. Newton diagrams for inelastic scattering of CD_3 with (a) D_2 and (b) H_2. The Newton spheres are drawn for inelastic scattering of CD_3 from the initial state $n_k = 0_0$ to the final state $n'_{k'} = 2_0$, which corresponds to an energy transfer of $\Delta E = 29.0$ cm^{-1} and for $\Delta j_2 = 0$ and $j_2 = 0$ to $j'_2 = 2$ transitions between rotational levels of D_2 and H_2.

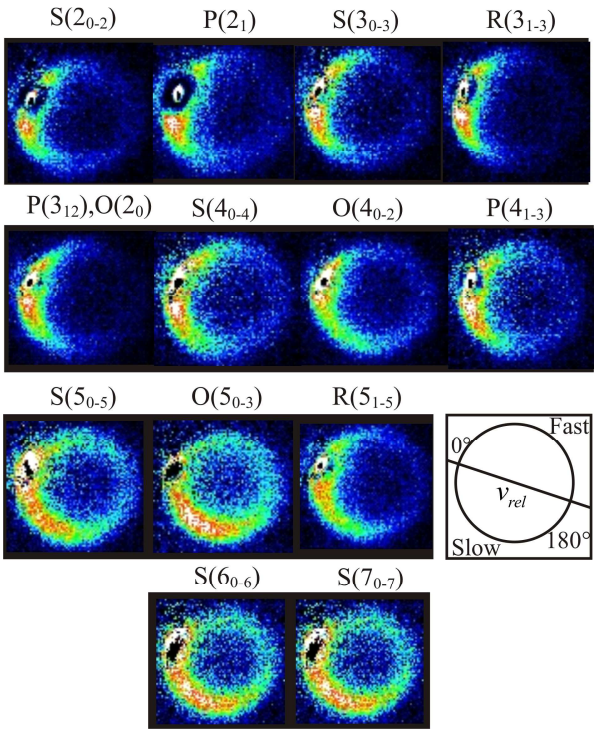

FIG. 6. Raw images for inelastic scattering of CD_3 radicals by D_2 at a collision energy of 640 ± 60 cm^{-1}. The images are labelled by the symbol Y($n'_{k'_1-k'_N}$) for final rotational levels with n' = 2 – 7 for the CD_3 radical, with unresolved final k' projection levels as discussed in section II.B. Y denotes the spectroscopic branch. The orientation of the relative velocity vector v_{rel} is indicated in one panel.

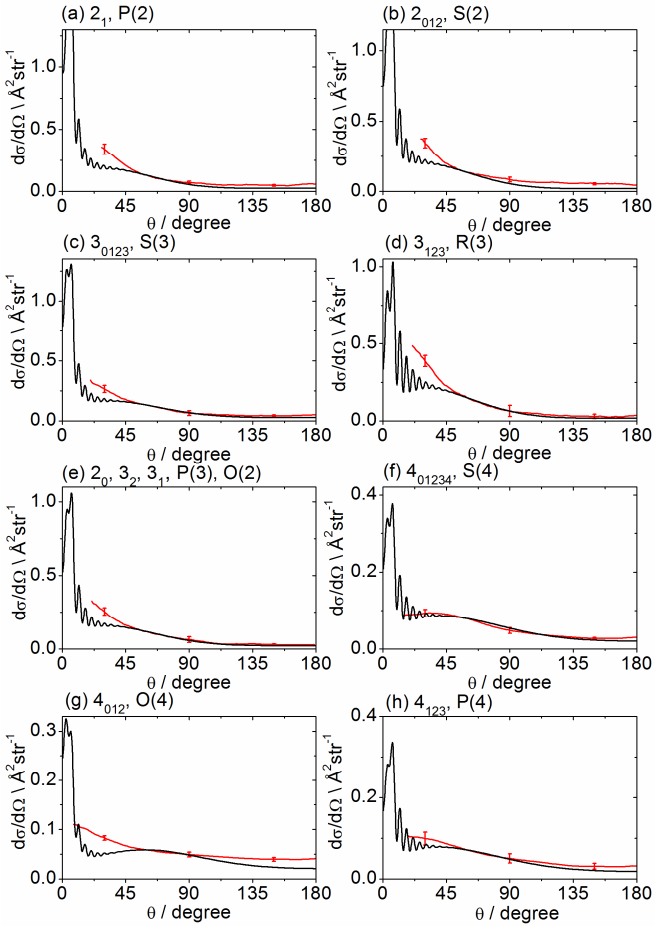

FIG. 7 Experimental (red) and theoretical (black) DCSs for inelastic scattering of CD_3 radicals by D_2 at a collision energy of 640 ± 60 cm^{-1} into final rotational levels $n' = 2 - 4$. The REMPI line employed for detection is indicated, along with the range of k' projection levels contributing to the scattering. The method of normalization of the experimental DCSs is described in the main text.

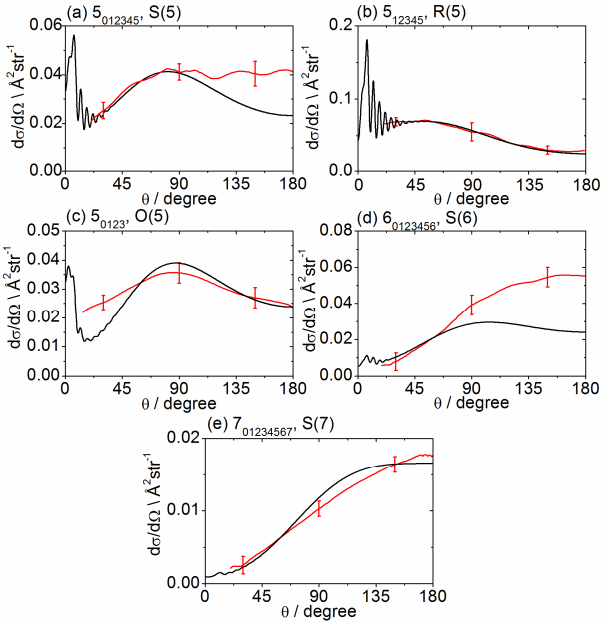

FIG. 8. Experimental (red) and theoretical (black) DCSs for inelastic scattering of CD_3 radicals by D_2 at a collision energy of 640 ± 60 cm^{-1} into final rotational levels $n' = 5 - 7$. The REMPI line employed for detection is indicated, along with the range of k' projection levels contributing to the scattering. The method of normalization of the experimental DCSs is described in the main text.

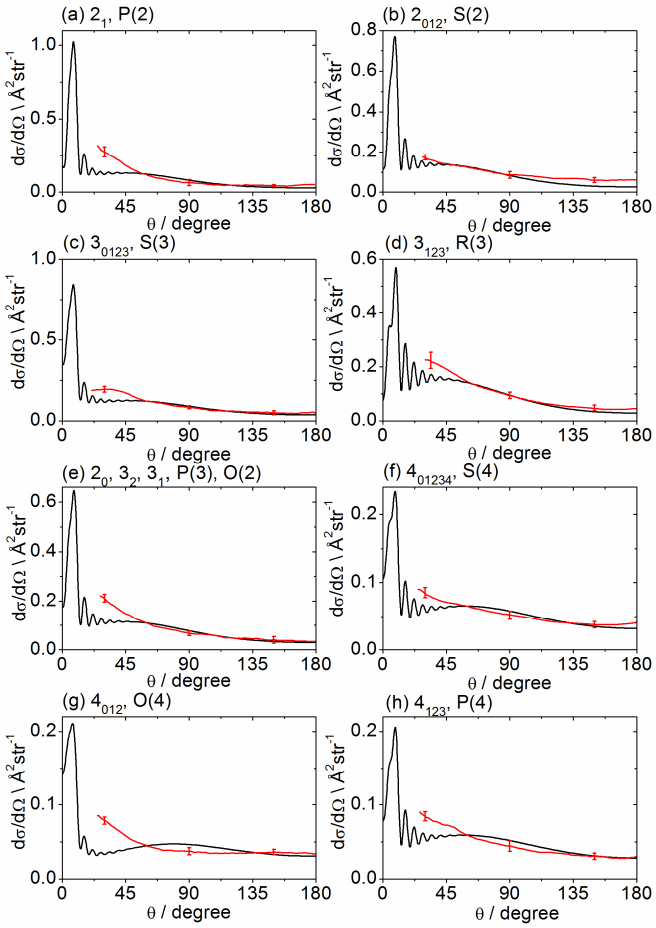

FIG. 9. Experimental (red) and theoretical (black) DCSs for inelastic scattering of CD_3 radicals by H_2 at a collision energy of 680 ± 75 cm^{-1} into final rotational levels $n' = 2 – 4$. The REMPI line employed for detection is indicated, along with the range of k' projection levels contributing to the scattering. The method of normalization of the experimental DCSs is described in the main text.

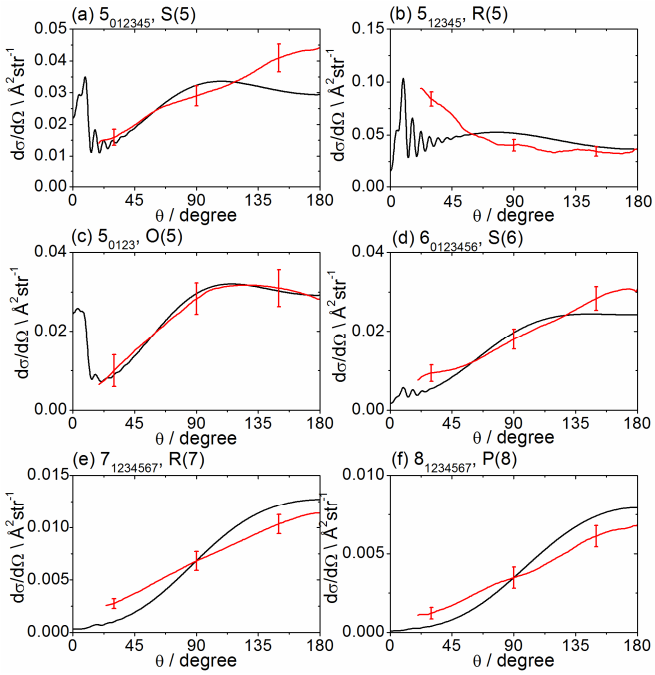

FIG. 10. Experimental (red) and theoretical (black) DCSs for inelastic scattering of CD_3 radicals by H_2 at a collision energy of 680 ± 75 cm^{-1} into final rotational levels $n' = 5 - 8$. The REMPI line employed for detection is indicated, along with the range of k' projection levels contributing to the scattering. The method of normalization of the experimental DCSs is described in the main text.

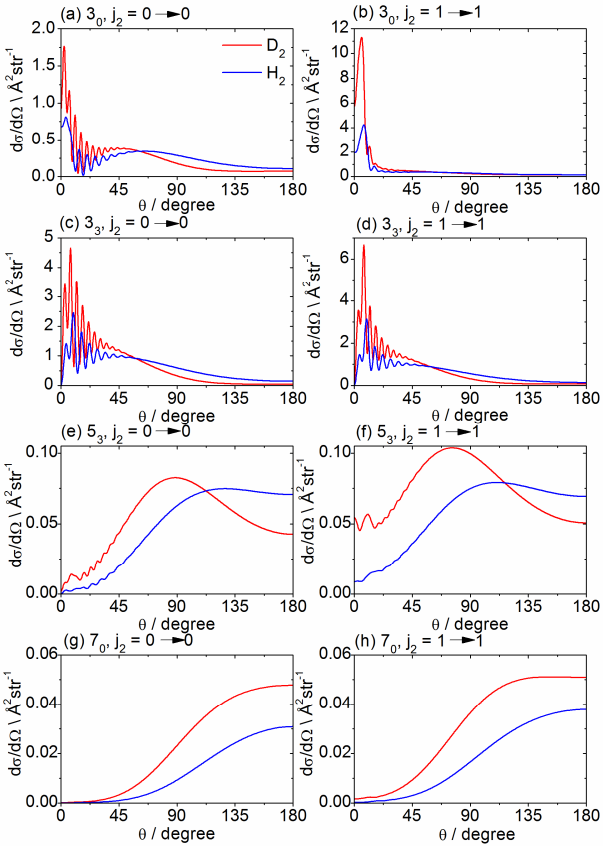

FIG. 11. Computed state-to-state DCSs for inelastic scattering of CD_3, initially in the 1_0 rotational level, with D_2 (red) and H_2 (blue) into selected final rotational levels at collision energies of 640 and 680 cm^{-1}, respectively. The left and right panels are DCSs for which the initial rotational level j_2 of the collision partner equals 0 and 1, respectively, and is the same after the collision.

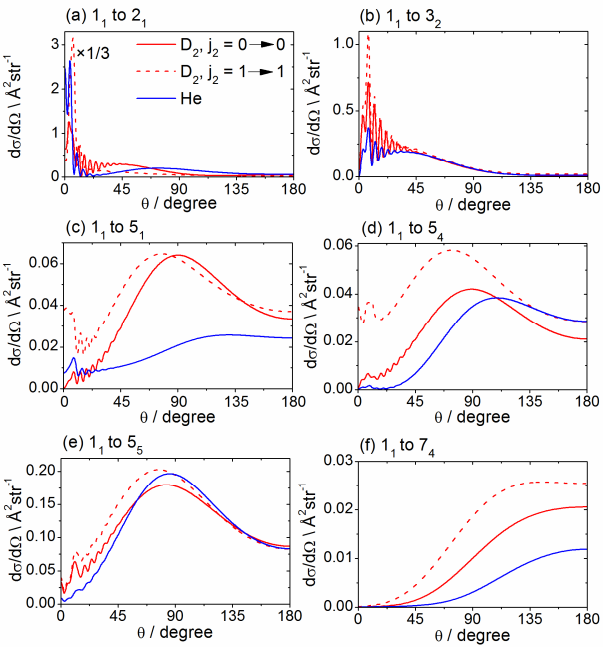

FIG. 12. Computed state-to-state DCSs for inelastic scattering of CD_3 from the 1_1 rotational level into various final rotational levels in collisions with D_2 (red) and He (blue) at a collision energy of 640 cm^{-1}. The solid and dashed red curves are CD_3–D_2 DCSs for which the initial rotational level j_2 of the D_2 collision partner equals 0 and 1, respectively, and is the same after the collision. In panel (a), the $j_2 = 1 \rightarrow 1$ DCS has been multiplied by a factor of 1/3.